

Dark and Baryonic Matter in Bright Spiral Galaxies: I. Near-infrared and Optical Broadband Surface Photometry of 30 Galaxies¹

Susan A. Kassin^{2,3}, Roelof S. de Jong⁴, & Richard W. Pogge²

ABSTRACT

We present photometrically calibrated images and surface photometry in the B , V , R , J , H , and K -bands of 25, and in the g , r , and K -bands of 5 nearby bright ($B_T^o < 12.5$ mag) spiral galaxies with inclinations between 30–65 degrees spanning the Hubble Sequence from Sa to Scd. Data are from The Ohio State University Bright Spiral Galaxy Survey, the Two Micron All Sky Survey, and the Sloan Digital Sky Survey Second Data Release. Radial surface brightness profiles are extracted, and integrated magnitudes are measured from the profiles. Axis ratios, position angles, and scale lengths are measured from the near-infrared images. A 1-dimensional bulge/disk decomposition is performed on the near-infrared images of galaxies with a non-negligible bulge component, and an exponential disk is fit to the radial surface brightness profiles of the remaining galaxies.

Subject headings: galaxies: general – galaxies: fundamental parameters – galaxies: photometry – galaxies: spiral – galaxies: stellar content

1. Introduction

The main uncertainty in the determination of the distribution of dark matter in galaxies from their rotation curves stems from the poorly known stellar mass distribution of galaxies (e.g., Verheijen 1997). In the cur-

rently fashionable picture of galaxy formation in a cold dark matter universe, both dark and luminous matter are expected to make a measurable contribution to the total mass in the inner parts of bright spiral galaxies. The relative contributions of luminous and dark matter have so far been poorly constrained due to uncertainty in the mass scaling of the stellar component, and the ensuing degeneracies between the stellar mass and dark matter contributions (e.g., Barnes et al. 2004). Recently, it has been shown that the uncertainty in the stellar component can be reduced by the inclusion of multi-band photometry, preferably with at least one near-infrared passband to abate the effects of dust on the determination of the stellar populations present (Bell & de

¹Based in part on observations obtained at the Cerro Tololo Interamerican Observatory, operated by the Association of Universities for Research in Astronomy, Incorporated, under a cooperative agreement with the National Science Foundation.

²Department of Astronomy, The Ohio State University, 140 W. 18th Ave., Columbus, OH 43210-1173

³currently at: UCO/Lick Observatory, University of California, Santa Cruz, CA 95064; kassin@ucolick.org

⁴Space Telescope Science Institute, 3700 San Martin Dr., Baltimore, MD 21218

Jong 2001).

The color versus mass-to-light ratio relations of stellar populations described by Bell & de Jong (2001) are affected by dust attenuation. It is known from detailed dust models (e.g., Disney, Davies, & Phillipps 1989, Gordon et al. 2001, Witt, Thronson, & Capuano 1992) that the effects of dust on the surface brightness profiles and integrated magnitudes of galaxies (extinction and scattering) are regulated by the geometry of stars and dust in the galaxies. Because this geometry is unknown, we cannot know the exact effects of dust on the galaxies' surface brightness profiles and integrated magnitudes. However, to first order, errors in the dust reddening estimates are not expected to strongly affect the masses derived from broadband colors of stellar populations. The dust will systematically both redden and extinguish galactic light, making a galaxy appear dimmer and to have a larger stellar mass-to-light ratio than it should. These effects work in opposite directions, so that errors in extinction corrections lead only to small errors in the derived stellar masses. The effects of dust on the derivation of stellar masses from photometry are discussed in depth in a subsequent paper (hereafter Paper II; Kassin et al., accepted).

With a better determination of the stellar mass distribution, one can place tighter constraints on the dark matter component of galaxies by comparing the luminous components of a galaxy (stars and gas) to total dynamical mass distributions derived from rotation curves. In this paper, we present optical and near-infrared photometry for a sample of galaxies that have rotation curves available in the literature. We use these data, along with surface brightness profiles from Verheijen (1997), the Sloan Digital Sky Survey Second Data Release Abazajian et al. (SDSS DR2; 2004), and the Two Micron All Sky Survey (2MASS; Jarrett et al. 2000; Cutrie et al.

2000; Jarrett et al. 2003) to determine the distributions of luminous and dark matter for 34 galaxies in Paper II. With this data in hand, we also investigate the angular momentum content of the 34 galaxies in Kassin et al., (in preparation) (Paper III).

Historically, galaxies have been studied with broad-band photometry at optical wavelengths, while more recent studies have extended into the near-infrared. Whereas optical bands are most sensitive to young Population I blue stars which account for only a small fraction of the total stellar mass of a galaxy, near-infrared bands give a much better census of the older stars which play a greater role in determining the stellar mass of a galaxy. Moreover, the extinction due to dust is much less at near-infrared than at optical wavelengths. Extinction at the near-infrared *K*-band is only about 10% of that at the optical *B*-band (Martin & Whittet 1990). Numerous studies have focused on near-infrared photometry of local spiral galaxies (e.g., de Jong & van der Kruit 1994; Héraudeau & Simien 1996; Gavazzi et al. 2003; Knapen et al. 2003; Jarrett et al. 2003). However, of these, only the Verheijen (1997) sample of both high and low surface brightness galaxies in Ursa Major includes dynamical information. The sample presented here encompasses non-interacting, large, bright, spiral galaxies, for which most theories of galaxy formation and evolution make predictions, and which are useful for probing the spiral galaxy Hubble Sequence.

This paper is organized as follows: The details of our sample selection, observation, reduction, and calibration are discussed in §2–4. The calculation of physical parameters for each of the galaxies is discussed in §5. Our photometry and radial surface brightness profiles are compared with those in the literature in §6. Distances are calculated in §7, and a very brief summary of our data is presented in §8. Throughout this paper we adopt a Hub-

ble constant of $H_0 = 70 \text{ km s}^{-1} \text{ Mpc}^{-1}$. When distance-dependent quantities have been derived from the literature, we have converted them using this value of H_0 .

2. Sample Selection

The sample encompasses a total of 30 galaxies from The Ohio State University Bright Spiral Galaxy Survey (OSUBSGS; Eskridge et al. 2002), 2MASS, and the SDSS DR2 which span the Hubble Sequence of spirals from Sa to Scd for bright galaxies ($B_T^o < 12.5 \text{ mag}$). Table 1 lists all the galaxies in the sample, their morphological class, $\mu_B = 25 \text{ mag arcsec}^{-2}$ isophotal diameter (D_{25}) from de Vaucouleurs et al. (1991) (hereafter, RC3), D_{25} measured from data in this paper, heliocentric radial velocity (V_{hel}), and adopted distance. Uncertainties in D_{25} due to both errors in fits to the exponential disks and zero-point calibrations are typically $\sim 5 \text{ arcsec}$. Parameters of the five galaxies from the Verheijen (1997) sample that will be used in the subsequent analyses are also listed. Of the galaxies studied in this paper, 25 have imaging in at least one band from the 2MASS, and 5 have optical imaging from the SDSS DR2. We use 2MASS K -band data to flux calibrate the OSUBSGS near-infrared images, and in some cases, to replace them. For one galaxy, NGC 3319, quality imaging at K is not available, so we use a 2MASS H -band image to calibrate its H -band image from the OSUBSGS.

The OSUBSGS is a sample of nearly 200 nearby bright spiral galaxies. Galaxies in this survey were chosen from the RC3 to have $1 \leq T_{RC3} \leq 7$ where T_{RC3} is the mean numerical Hubble stage index as tabulated in the RC3, $B_T^o \leq 12 \text{ mag}$, $D_{25} \leq 6.5 \text{ arcminutes}$ where D_{25} the apparent major isophotal diameter measured at $\mu_B=25 \text{ mag arcsec}^{-2}$, and $-80 < \delta < +50 \text{ degrees}$ where δ the declination (due to the pointing limits of

the Cerro Tololo Interamerican Observatory (CTIO) 1.5-meter and the Lowell Observatory Perkins 1.8-meter telescopes). We imposed a few additional criteria to select galaxies from the OSUBSGS: galaxies were required (1) to be non-interacting, (2) within an optimal inclination range ($\sim 30\text{--}\sim 65 \text{ degrees}$) in order to reduce the effect of dust extinction and reddening while still being able to obtain accurate kinematical information, (3) to have Galactic latitudes where the absorption due to our Galaxy is quantified in Schlegel, Finkbeiner, & Davis (1998), (4) to have a photometric optical calibration in the OSUBSGS, (5) to have a photometric near-infrared calibration in the OSUBSGS or the 2MASS, (6) and, to have a rotation curve available from the literature.

Galaxies were selected from the SDSS DR2 and 2MASS surveys if they had (1) sufficient quality imaging to create a high signal-to-noise surface brightness profiles at g, r , and K , (2) $B_T^o < 12 \text{ mag}$ to satisfy the selection criterion of the OSUBSGS, and satisfy the requirements for galaxies to be selected from the OSUBSGS.

3. Observations and Reduction for the OSUBSGS Galaxies

Data for the OSUBSGS were obtained during a large number of observing runs with six telescopes of apertures between 0.9 and 1.8 meters during the period 1993–2000. Table 2 lists the telescope, instrument, and detector used for each final image in our sample, along with the date each image was taken. The observations were made by the OSUBSGS team and their students, as well as by a professional observer (Roberto Aviles) hired by the project at CTIO. For details about the telescopes and instruments used and the manner in which the observations were taken, see Eskridge et al. (2002).

4. Photometric Calibration

4.1. OSUBSGS & 2MASS Galaxies

OSUBSGS observing nights were judged to be photometric in three stages. First, at the telescope the observer made a decision based on the weather and acquired standard star images if the night was apparently photometric. Second, the standard star data were reduced and if it was verified that the residuals between the observed and cataloged standard star magnitudes did not change during the night was flagged as possibly photometric. Finally, the photometric zero-points for contiguous nights were checked for consistency. If the zero-points for a night were not consistent with adjoining nights, and there was no change to the observing set-up (i.e., instrument changes between nights) that could account for the difference, then the night was judged to be non-photometric, and images from those nights were excluded from further consideration. If the zero-points for a night were consistent with adjoining nights, and there was no change in the observing set-up, then the night was judged to be photometric.

For the optical photometric calibration, equatorial standard star fields from Landolt (1992) were observed at a range of airmasses to derive photometric transformations onto the Kron-Cousins BVR system. Photometric zero-points, airmass terms, and $B - V$ color terms were calculated for each night with the `fitparams` task in IRAF. For each night, a photometric solution was fit to the standard star observations which included both airmass and $B - V$ color terms. Standard star observations which were outliers to this solution were examined and generally were found to be problematic due to factors such as cosmic ray contamination, bad pixels, bad columns/rows, or because some stars were imaged near the edges of the detectors. The

uncertainties given include those in the photometric calibration, in the measurement of instrumental magnitudes (which are dominated by sky variation), and that due to the fact that a galaxy does not color-correct like a star (unless each pixel of its image were individually color-corrected).

OSUBSGS J , H , and K -band images were photometrically calibrated with data from 2MASS. An attempt was made to use standard stars from the list of Carter & Meadows (1995), but due to ambiguities in the data we decided to calibrate them against the 2MASS database instead. To calibrate the 2MASS images, the zero-points listed in the 2MASS image headers were applied to the images.

J_{2MASS} , H_{2MASS} , and $K_{S,2MASS}$ were transformed to J_{CIT} , H_{CIT} , and K_{CIT} in order to calibrate the OSUBSGS near-infrared images that are on the CIT photometric system. The transformations used are the ones tabulated on the 2MASS website³ (where we leave out a color term that contributes as 0.001 mag):

$$J_{CIT} = K_{S,2MASS} + (0.019 \pm 0.004) \quad (1)$$

$$J_{CIT} = K_{CIT} + \frac{(J - K_S)_{2MASS} + 0.02}{1.068} \quad (2)$$

$$H_{CIT} = K_{CIT} + (H - K_S)_{2MASS} - 0.034. \quad (3)$$

We calibrated the near-infrared OSUBSGS images to the 2MASS images by comparing surface brightness profiles of galaxies extracted from both surveys in the same manner. We explain in detail the extraction of these profiles in Paper II. Surface brightness profiles from the OSUBSGS were calibrated to 2MASS profiles by finding the best-fit combination of a sky determination and magnitude zero-point that allows for the smallest difference between the profiles. The OSUBSGS profiles generally have poorer sky measurements, but they have higher signal-to-

³<http://www.astro.caltech.edu/~jmc/2mass/v3/transformations/>

noise ratios in their inner parts, and extend to larger galactocentric radii essential for the subsequent analysis. On average, the OSUBSGS infrared images have limiting surface brightnesses of ~ 2 mag arcsec $^{-2}$ fainter than those from 2MASS. However, in some cases, the 2MASS images are of better overall quality than the OSUBSGS images. In those cases, we adopt the 2MASS image for the final dataset. The calibration was done by plotting the calibrated flux from a 2MASS profile against the instrumental counts from an OSUBSGS profile. A straight line was fit to these data. The slope of this line determines the bootstrap zero-point necessary to calibrate the OSUBSGS image, and its intercept determines the sky offset multiplied by the zero-point. This procedure works well since, for a typical galaxy in the sample, the near-infrared color terms are small ($\sim 1\%$).

The photometric zero-point calibration of the 2MASS galaxies is accurate to $\pm 2\%$ – 3% (Cutrie et al. 2000). However, as warned in Appendix A of Jarrett et al. (2000), a small fraction of the galaxies may be affected by high-frequency background variations, causing the photometric error to increase. This does not appear to be the case in those galaxies presented here. The sky variation in our near-infrared images causes a further $\sim 2\%$ uncertainty in the photometric calibration. In total, the near-infrared calibrations are uncertain to $\sim 4\%$.

4.2. SDSS DR2 Galaxies

For the SDSS DR2 images, the zero-point calibration is accurate to $\pm 2\%$ in both SDSS r and SDSS $g - r$ (Lupton et al. 2001); the sky variation in our galaxy images causes a further $\sim 2\%$ uncertainty. In total, the zero-point calibration is uncertain by $\sim 4\%$. For these SDSS DR2 galaxies, we applied the zero-points and extinction terms as given in the “best TsField” FITS table.

5. Surface Brightness Profiles and Physical Properties of the Galaxies

5.1. Axis Ratios & Position Angles

In order to create surface brightness profiles, we first determined the axis ratio and position angle of each galaxy. (For galaxies with SDSS DR2 and 2MASS images, we adopted the position angles and axis ratios used in the literature for measuring their rotation curves.) Axis ratios and position angles were measured from H -band images of the galaxies. The H -band was chosen to measure physical parameters, because near-infrared wavelengths trace most of the stellar mass in galaxies, and our H -band images generally have higher signal-to-noise than our J or K images. For each H -band image of a galaxy, ellipses were fit with increasing semi-major axis from the galaxy’s center. This was done with the `profile` command in the XVista⁴ package, which uses a modification of Kent (1983)’s implementation of the azimuthal Fourier moments technique as described by Lauer (1985). The resulting plots of position angles and axis ratios of the ellipses versus radius were examined by eye, and a position angle and inclination were chosen for each galaxy at radii where the galaxy’s disk was exponential (usually between 2 and 3 scale lengths). As a check on the adopted parameters, an ellipse with the chosen axis ratio and position angle was plotted over the H -band image and visually inspected. This procedure was repeated until the parameters derived for each galaxy passed a visual inspection. The goal was to find the parameters that best follow the main structure of the galaxies’ stellar mass distributions. The measured axis ratio is converted into an inclination angle, i , under the assumption that the disks are in-

⁴XVista is based on Lick Observatory Vista and maintained by a loose consortium of die-hard users at <http://ganymede.nmsu.edu/holtz/xvista>.

trinsically circular ($q = \cos i$, where q is the ratio of minor and major axes). The final position angles and inclinations adopted for the galaxies are presented in columns 7 and 8 of Table 3. The typical errors in the position angles and inclinations are both approximately ± 5 degrees.

5.2. Radial Surface Brightness Profiles

To extract surface brightness profiles for each of our sample galaxies we used the XVista command `annulus`. The SDSS DR2 galaxies were first aligned to the World Coordinate System so that they were aligned with their respective 2MASS images. The `annulus` command computes a radial surface brightness profile by finding the median surface brightness per pixel in elliptical annuli of increasing distance from the center of a galaxy. We chose to calculate the median (instead of the mean) surface brightness in order to avoid foreground stars and effects such as bad pixels which tend to corrupt the average statistic. Ellipse parameters were predetermined for each galaxy, as discussed in §5.1, and centers were defined as the pixel in the nucleus with the highest surface brightness.

The resulting surface brightness profiles for each galaxy are presented in Figure 1, alongside their B and K -band images (K_S for 2MASS images) to allow for comparison of surface brightness profiles with morphological properties. The profiles have been corrected for Galactic extinction using Schlegel et al. (1998). The galaxies NGC 1090, NGC 2841, and NGC 3198 have SDSS DR2 images in which almost half of the galaxy is not present, as can be observed in the g -band images in Figure 1. This is also the case, but to a much lesser extent, for NGC 3521. We use the areas common to all passbands to create color profiles.

Total magnitudes and magnitudes within

the $\mu_B = 25$ mag arcsec $^{-2}$ isophotal radius (R_{25}) were measured by integrating the surface brightness profiles to R_{25} , extrapolating the profiles with an exponential function when necessary. The resulting magnitudes are listed in columns 4 and 5 of Table 3 along with magnitudes from the literature in column 7 for comparison. Note that Verheijen (1997)’s K' -band measurements have not been converted to K_{CIT} since the difference between the two bands is small (~ 0.05 mag for typical mean $J - H$ colors). The seeing for each image is listed in column 3 of Table 3; the typical error in the seeing is $\pm 0.2''$.

5.3. Bulge/Disk Decompositions

The radial surface brightness profiles in the H or K -band for each of the galaxies were decomposed into bulge and disk components following de Jong (1996) and Knapen et al. (2003) (see also MacArthur, Courteau, & Holtzman 2003). The bulge component was fit using a generalized Sérsic (1968) profile of the form

$$\mu(R) = \mu_e + 2.5b_n \left[\left(\frac{R}{R_e} \right)^{1/n} - 1 \right] \quad (4)$$

where n is the bulge shape parameters ($n = 4$ for a deVaucouleurs $r^{1/4}$ law, $n = 1$ for an exponential disk), R_e is the effective radius, μ_e is the surface brightness at R_e , and b_n is a normalization factor depending on n that ensures that half of the integrated light is within R_e . Only n , R_e , and μ_e are free parameters. The disk was fit with a standard exponential surface brightness profile of the form

$$\mu(R) = \mu_0 + 1.086(R/h) \quad (5)$$

where μ_0 is the central surface brightness of the disk and h is the disk scale length.

The results for the 5-parameter bulge/disk fits to our near-infrared radial surface-brightness profiles are summarized in Table 4. The

bulge-to-disk ratio (B/D) was derived from integrating the best fit bulge and disk profiles, and is listed in Table 4. For 20 galaxies, the added bulge component did not change the predicted stellar mass rotation curves beyond the uncertainties in our adopted mass-to-light ratios (see Paper II) compared to the one derived for the disk alone. We re-fit these galaxies solely with an exponential disk. Not surprisingly, these galaxies are all among the latest Hubble types in this sample.

Note that the disk parameter measurements made here do not depend on the outer parts of the surface brightness profiles where uncertainties in the sky determination have the most effect. The outer parts of the surface brightness profiles (where the signal-to-noise drops below $\sim 1\sigma$) were removed for the bulge/disk decompositions and exponential disk fits. Because of this, the effect of uncertainties in the sky determination also do not affect the bulge parameters.

6. Comparison With Photometry and Radial Surface Brightness Profiles in the Literature

In Figure 2, surface brightness profiles are compared with those from the literature and SDSS DR2. We do not compare the near-infrared profiles since they are calibrated to 2MASS. We plot in Figure 2 the radial difference between the literature magnitude and the magnitude derived in this paper. In each of the panels of the figure, the bands of the surface brightness profiles compared are noted beneath the galaxy’s NGC number: the bands of the profiles from this paper are written first, then those from the literature next. Aside from the SDSS DR2 comparisons, those from the literature are from: Ryder et al. (1998) for NGC 157, Mathewson, Ford, & Buchhorn (1992) for NGC 908, NGC 1241, NGC 1385, NGC 1559, NGC 1832, NGC 2090, NGC 2139, NGC 7083, and NGC 7606, Héraudeau &

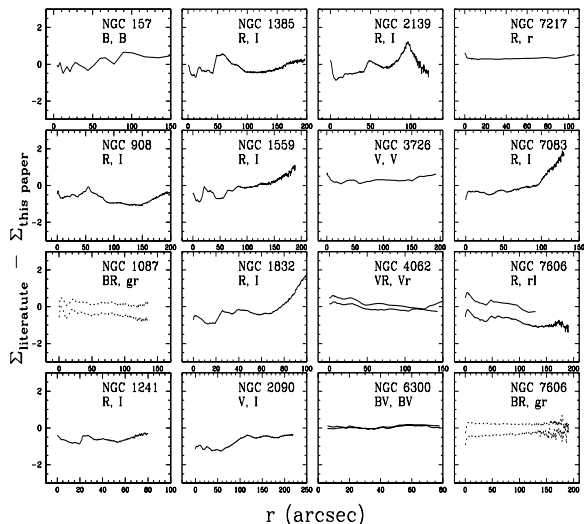


Fig. 2.— Surface brightness profiles from this paper are compared to those in the literature (solid lines) and the SDSS DR2 (short dashed lines). Under the galaxy’s NGC number, the band(s) of the surface brightness profile(s) plotted from this paper is(are) noted first, then the band(s) from the literature/SDSS DR2 are(are) noted after.

Simien (1996) for NGC 3726 and NGC 4062, Kent (1986) for NGC 4062, NGC 7217, and NGC 7606, and Buta (1987) for NGC 6300.

For the SDSS DR2, we compare the g and r -band (AB magnitudes) surface brightness profiles with those for the B and R -bands (Vega magnitudes) measured in this paper. There is an offset from zero for all the curves. For NGC 1087 and NGC 7606, on average, the offsets for $g - B$ are 0.45 and 0.36 mag, and those for $r - R$ are 0.18 and 0.22, respectively. This is consistent with the expected colors of galaxies from the 1996 version of the Bruzual & Charlot 2003 GISSEL models (Bruzual & Charlot 1993) for exponentially declining star-formation rates: $g - B \sim -0.38$ and $r - R \sim 0.22$ for a typical galaxy color of $V - R = 0.5$. There is not a large difference between the sky subtraction of the SDSS pro-

files and those presented in this paper since the sky values in both images were both calculated with the same technique.

The difference between the *I*-band profiles measured by Mathewson et al. (1992) and the *R*-band profiles from this paper is within the spread of *R* – *I* colors of spiral galaxies (de Jong & van der Kruit 1994). The difference for *V* compared with *I* for NGC 2090 is similarly within the spread of *V* – *I* colors given in de Jong & van der Kruit (1994). The Mathewson et al. (1992) profiles are consistent with those presented in this paper even though the methods that are used to compute them differ. Those from this paper are computed in a fixed ellipse determined from an outer isophote of an *H*-band image, whereas those in Mathewson et al. (1992) are computed in ellipses whose position angles and inclinations are allowed to vary on the *I*-band images. A difference in profile extraction can also cause differences in the shapes of the surface brightness profiles, especially when dealing with bars and rings. Also, the Mathewson et al. (1992) data have systematically higher sky values as evidenced by the upturn at the ends of the curves in Figure 2. Differences in sky subtraction are most apparent in the outer parts of the profiles since it is there that the source counts become comparable to the sky counts. A difference in the methods of sky determination may account for the differences in sky subtraction. We calculate the sky counts in our images by using the XVista command `sky` in boxes inside the images where the contribution from the galaxies is small. This command finds the sky background level under the assumption that the most common pixel value in the chosen box is the sky value. In particular, the `sky` routine calculates the mean of the pixel values in the box, and builds a histogram of the values about the mean. The region of the peak pixel value is located in the histogram by fitting it with a parabola.

The center of this parabola is taken as the sky value. Mathewson et al. (1992) measured the sky by calculating the mode pixel value in a 127 pixel wide boarder around each frame. Also, the regions where the sky value was calculated in Mathewson et al. (1992) may have been contaminated by galaxy counts.

For comparisons with literature references other than SDSS DR2 and Mathewson et al. (1992), the profiles are consistent. For NGC 157, the profiles are consistent to within 0.05 mag, which is within their uncertainties. However, the sky measurements differ between the two profiles. Sky measurements were made by Ryder et al. (1998) by using the modal peak of the histogram of data values within 20 pixels of the image edges, similar to the method used in this paper. Therefore, we should not expect a difference between the sky measurements. The integrated magnitude of NGC 157 from Ryder et al. (1998) is also fainter than the integrated magnitude given in this paper (which is consistent the RC3 measurement). For NGC 3726, we compare the *V*-band profiles and find a 0.30 mag difference on average. This is consistent with the uncertainties: the uncertainty given by Héraudeau & Simien (1996) is 0.02 mag for the rms error due to the sky value uncertainty, the zero-point uncertainty from Héraudeau & Simien (1996) is estimated to be within 0.1–0.3 mag, and the zero-point uncertainty for the profile presented in this paper is 0.06 mag. For NGC 4062, the average difference from the literature is 0.06 mag, which is within uncertainties. For NGC 6300, the *B* and *V* profiles are compared with profiles of the same bands from the literature, and the differences are found to be 0.05 and 0.06 mag, respectively, consistent with zero-point uncertainties. The galaxies NGC 4062, NGC 7217, and NGC 7606 have average offsets between the *R*-band profiles given here and the *r*-band profiles given in Kent (1983) of 0.34, 0.33, and 0.36 mag,

respectively. These differences are consistent with the expected colors of typical galaxies in this paper (see paragraph on SDSS comparison) if zero-point uncertainties are taken into account.

In Table 3, we list integrated magnitudes from the literature for many of the galaxies in our sample. We plot the difference between total magnitudes from the RC3 and those presented in this paper in Figure 3a,b for the B and V -bands, respectively. For the B -band, we find a mean difference of 0.13 mag with a σ of 0.33 mag. For the V -band, there are only 4 galaxies with a measurement in the RC3. For this band, there is no mean difference between the magnitudes presented here and in the RC3, but there is a σ of 0.29 mag. The zero-point differences of these comparisons are within the expected errors, but the high σ values are somewhat disturbing. Those galaxies with large differences between zero-points are NGC 289 (differences of 0.67 mag for B and 0.55 mag for V), NGC 1241 (0.89 mag for B), and NGC 2280 (0.90 for B). For NGC 289, the V -band magnitude given for data in this paper, while not consistent with the RC3, is consistent with that of Walsh, Staveley-Smith, & Oosterloo (1997). Similarly, for NGC 1241, the R -band surface brightness profile given in this paper is consistent with the I -band profile from Mathewson et al. (1992). And, for NGC 2280, the B -band magnitude is consistent with that of Lauberts & Valentijn (1989).

Other integrated magnitude measurements from the literature are for NGC 157 from Ryder et al. (1998) (discussed above), NGC 3726, NGC 4062, NGC 4651, and NGC 7606 from Héraudeau & Simien (1996), and NGC 6300 from Buta (1987). For NGC 4062, NGC 4651, and NGC 7606, the magnitudes are consistent. The differences between the integrated magnitudes of NGC 6300 given here and in the literature are likely due to the myriad foreground stars contaminating its image. In-

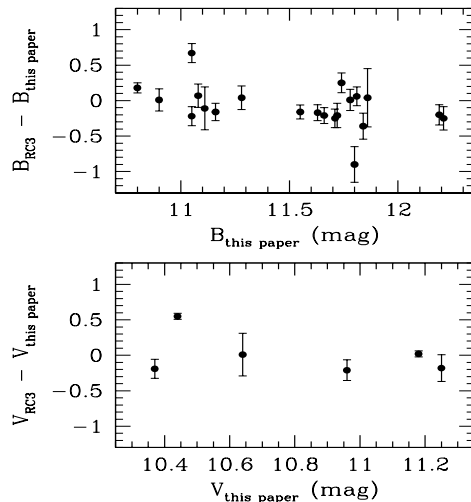


Fig. 3.— We plot the difference between the total integrated RC3 magnitudes and the integrated magnitudes from this paper versus magnitudes from this paper. In the upper panel we compare the B -band magnitudes, and in the lower panel we compare the V -band magnitudes.

tegrated magnitudes given in the literature for NGC 6300 are calculated by removing a few field stars from the image and then using aperture photometry. Buta (1987) used photographic plates and they mention that “a wide range of apertures was used, but because of the lack of a conspicuous nucleus and the large number of foreground stars, it was not possible to obtain the maximum range achievable with the photographic equipment and telescopes used for the observing.” Integrated magnitudes are derived from the surface brightness profiles of NGC 6300 which were calculated with a median statistic. This allows us to avoid the problem of subtracting the myriad foreground stars in the image of NGC 6300. This difference can explain why the surface brightness profiles of NGC 6300 are consistent with those in the literature, while the integrated magnitudes are not.

7. Distances

Table 1 lists the distances for each of the galaxies in Megaparsecs (Mpc). These were calculated under the assumption of Hubble flow, after correction for Virgocentric infall, following the formalism of Aaronson et al. (1982). Four galaxies were found to have triple-valued solutions for their distances in the Virgocentric infall solution. For these galaxies, NGC 4062, NGC 4651, and NGC 4698, a distance was adopted based on *H*-band Tully-Fisher distances.

In addition, 4 galaxies in the sample have distances measured by Hubble Space Telescope (HST) observations of Cepheid variable stars: NGC 2090 (Phelps et al. 1998), NGC 2841 (Macri et al. 2001), NGC 3198 (Kelson et al. 1999), and NGC 3319 (Sakai et al. 1999). In all 4 cases, we have adopted these Cepheid distances, which are listed in Table 1. For those galaxies from Verheijen (1997), we adopt the HST Key Project distance to the Ursa Major cluster of 20.7 Mpc (Sakai et al. 2000).

8. Summary

Photometrically calibrated surface brightness profiles, magnitudes, and physical parameters are presented for a sample of 31 nearby bright spiral galaxies for which dynamical information is available in the literature.

SAK would like to acknowledge financial support from The Space Telescope Science Institute Director's Discretionary Research Fund (DDRF). We thank the referee, P. Grosbøl, for his thorough comments that helped improve the final version of this paper. We are grateful to Jay Frogel for initiating the OSUBSGS and to Don Terndrup for help with the optical calibrations used in this paper.

We thank the CTIO TAC for generous allocation of time for the OSU Galaxy Survey and

the many people over the years who helped collect these observations. Funding for the OSU Bright Spiral Galaxy Survey was provided by grants from The National Science Foundation (grants AST-9217716 and AST-9617006), with additional funding by The Ohio State University.

This paper makes use of data from both the Sloan Digital Sky Survey and the Two Micron All Sky Survey. The Two Micron All Sky Survey is a joint project of the University of Massachusetts and the Infrared Processing and Analysis Center/California Institute of Technology, funded by the National Aeronautics and Space Administration and the National Science Foundation. Funding for the creation and distribution of the SDSS Archive has been provided by the Alfred P. Sloan Foundation, the Participating Institutions, the National Aeronautics and Space Administration, the National Science Foundation, the U.S. Department of Energy, the Japanese Monbukagakusho, and the Max Planck Society. The SDSS Web site is <http://www.sdss.org/>. The SDSS is managed by the Astrophysical Research Consortium (ARC) for the Participating Institutions. The Participating Institutions are The University of Chicago, Fermilab, the Institute for Advanced Study, the Japan Participation Group, The Johns Hopkins University, Los Alamos National Laboratory, the Max-Planck-Institute for Astronomy (MPIA), the Max-Planck-Institute for Astrophysics (MPA), New Mexico State University, University of Pittsburgh, Princeton University, the United States Naval Observatory, and the University of Washington.

This research has made use of the NASA/IPAC Extragalactic Database (NED) that is operated by the Jet Propulsion Laboratory, California Institute of Technology, under contract with the National Aeronautics and Space Administration. This research has also made use of NASA's Astrophysics Data System.

Facilities: Perkins (OSIRIS,IFPS), CTIO:0.9m (CFCCD), CTIO:1.5m (CIRIM, CFCCD), Hiltner (MIS), McGraw-Hill (MIS)

REFERENCES

- Aaronson, M., Huchra, J., Mould, J., Schechter, P. L., & Tully, R. B. 1982, *ApJ*, 258, 64
- Abazajian, K. et al. 2004, *AJ*, 128, 502
- Bell, E. F. & de Jong, R. S. 2001, *ApJ*, 550, 212
- Barnes, E. I., Sellwood, J., A., & Kosowsky, A. 2004, *AJ*, 128, 2724
- Bruzual, A. G., & Charlot, S. 1993, *ApJ*, 405, 538
- Buta, R. 1987, *ApJS*, 64, 383
- Carter, B. S. & Meadows, V. S. 1995, *MNRAS*, 276, 734
- Cutri, R. M., et al. 2000, Explanatory Supplement to the 2MASS Second Incremental Data Release (Pasadena: Caltech)
- de Jong, R. S. & van der Kruit, P. C. 1994, *A&AS*, 106, 451
- de Jong, R. S. 1996, *A&AS*, 118, 557
- de Vaucouleurs, G., de Vaucouleurs, A., Corwin, H. G., Jr., Buta, R. J., Paturel, G., Fouque, P. 1991, *Third Reference Catalogue of Bright Galaxies, Version 3.9* (New York: Springer)
- Disney, M., Davies, J., & Phillipps, S. 1989, *MNRAS*, 239, 939
- Eskridge, P. B. et al. 2002, *ApJS*, 143, 73
- Gavazzi, G., Boselli, A., Donati, A., Franzetti, P., & Scodreggio, M. 2003, *A&A*, 400, 451
- Gordon, K. D., Misselt, K. A., Witt, A. N., & Clayton, G. C. 2001, *ApJ*, 551, 269
- Héraudeau, Ph & Simien, F. 1996, *A&A*, 118, 111
- Jarrett, T. H., Chester, T., Cutri, R., Schneider, S. E., Huchra, J. P. 2003, *AJ*, 125, 525
- Jarrett, T. H., Chester, T., Cutri, R., Schneider, S., Skrutskie, M., & Huchra, J. P. 2000, *AJ*, 119, 2498
- Kassin, S. A., de Jong, R. S., & Weiner, B. J. 2005, accepted (Paper II)
- Kassin, S. A. et al., in preparation (Paper III)
- Kelson, D. D. et al. 1999, *ApJ*, 514, 614
- Kent, S. M. 1983, *ApJ*, 266, 562
- Kent, S. M. 1986, *AJ*, 91, 1301
- Knapen, J. H., de Jong, R. S., Stedman, S., & Bramich, D. M. 2003, *MNRAS*, 344, 527
- Landolt, A. U. 1992, *AJ*, 104, 340
- Lauberts, A. & Valentijn, E. A. 1989, *The Surface Photometry Catalogue of the ESO-Uppsala Galaxies* (Garching: ESO)
- Lauer, T. R. 1985, *ApJS*, 57, 473
- Lupton, R. et al. 2001, in *ASP Conf. Ser. 238, Astronomical Data Analysis Software and Systems X*, ed. F. R. Harnden, Jr., F. A. Primini, and H. E. Payne (San Francisco: Astr. Soc. Pac.), 269
- MacArthur, L. A., Courteau, S., & Holtzman, J. A. 2003, *ApJ*, 582, 689
- Macri, L. M. et al. 2001, *ApJ*, 559, 243
- Martin, P. G. & Whittet, D. C. B. 1990, *ApJ*, 357, 113
- Mathewson, D. S., Ford, V. L., & Buchhorn, M. 1992, *ApJS*, 81, 413
- Phelps, R. L. et al. 1998, *ApJ*, 500, 763

- Ryder, S. D., Zasov, A. V., Sil'chenko, O. K., McIntyre, V. J., & Walsh, W. 1998, MNRAS, 293, 411
- Sakai, S. et al. 1999, ApJ, 523, 540
- Sakai, S. et al. 2000, ApJ, 529, 698
- Schlegel, D. J., Finkbeiner, D. P., & Davis, M. 1998, ApJ, 500, 525
- Sérsic, J. L. 1968, Atlas de Galaxias Australes (Cordoba, Argentina: Observatorio Astronomico)
- Tully, R. B. 1988, Nearby Galaxies Catalog (Cambridge: Cambridge Univ. Press)
- Verheijen, M. A. W. 1997, Ph.D. thesis, Rijksuniversiteit Groningen
- Walsh, W., Staveley-Smith, L., & Oosterloo, T. 1997, AJ, 113, 1591
- Witt, A. N., Thronson, H. A., & Capuano, J. M. 1992, ApJ, 393, 611

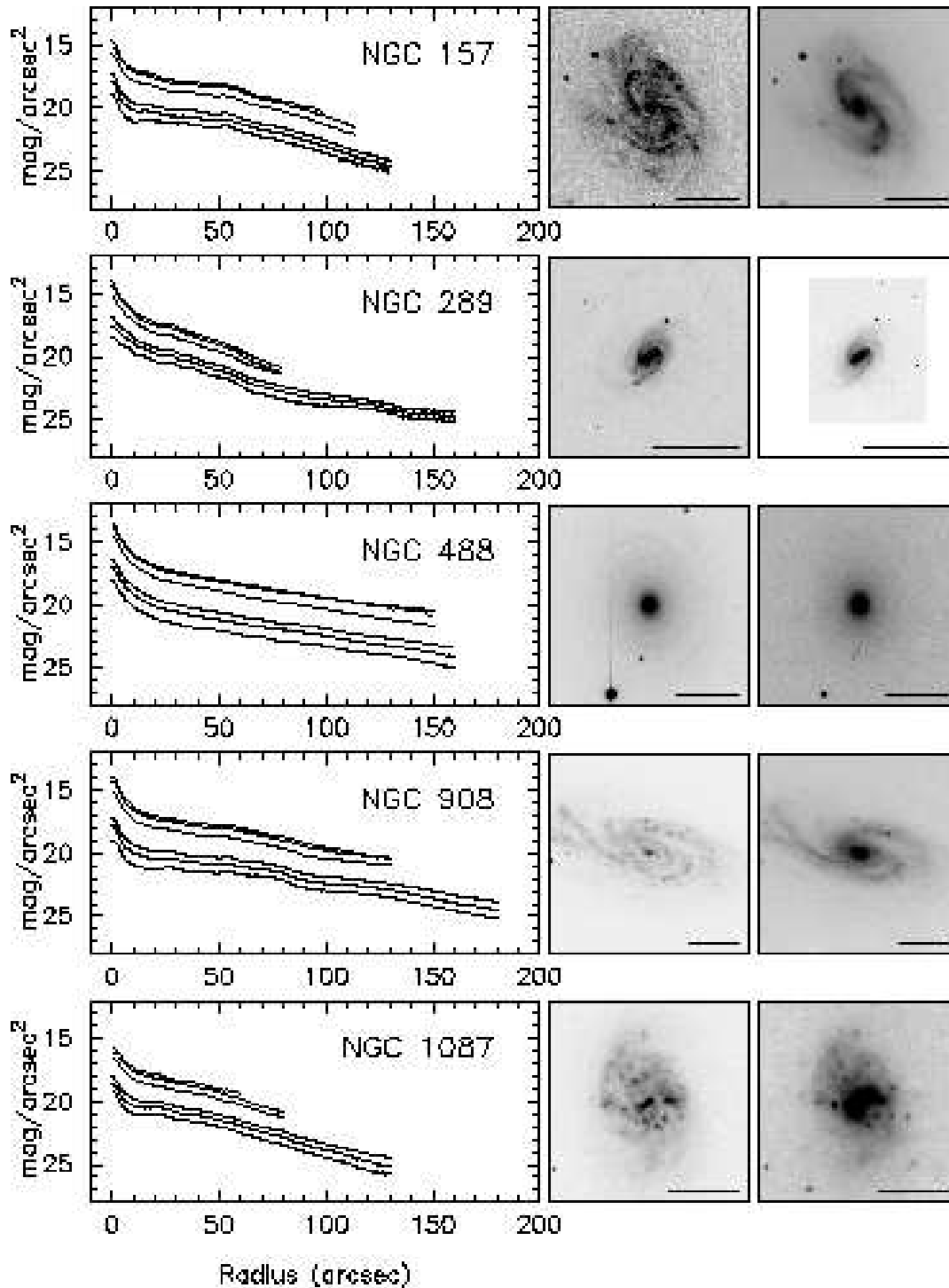


Fig. 1a.— Observed surface brightness profiles and B and K -band images for the sample galaxies. In this and subsequent figures, surface brightness curves run B-to-K bottom-to-top; see Table 2 for the observed bands. The B image is on the left, K on the right, and the scale bar indicates $60''$. Orientation is North=Up, East=Left. Degraded resolution for astro-ph; please see journal article or send an email for a version at a higher resolution.

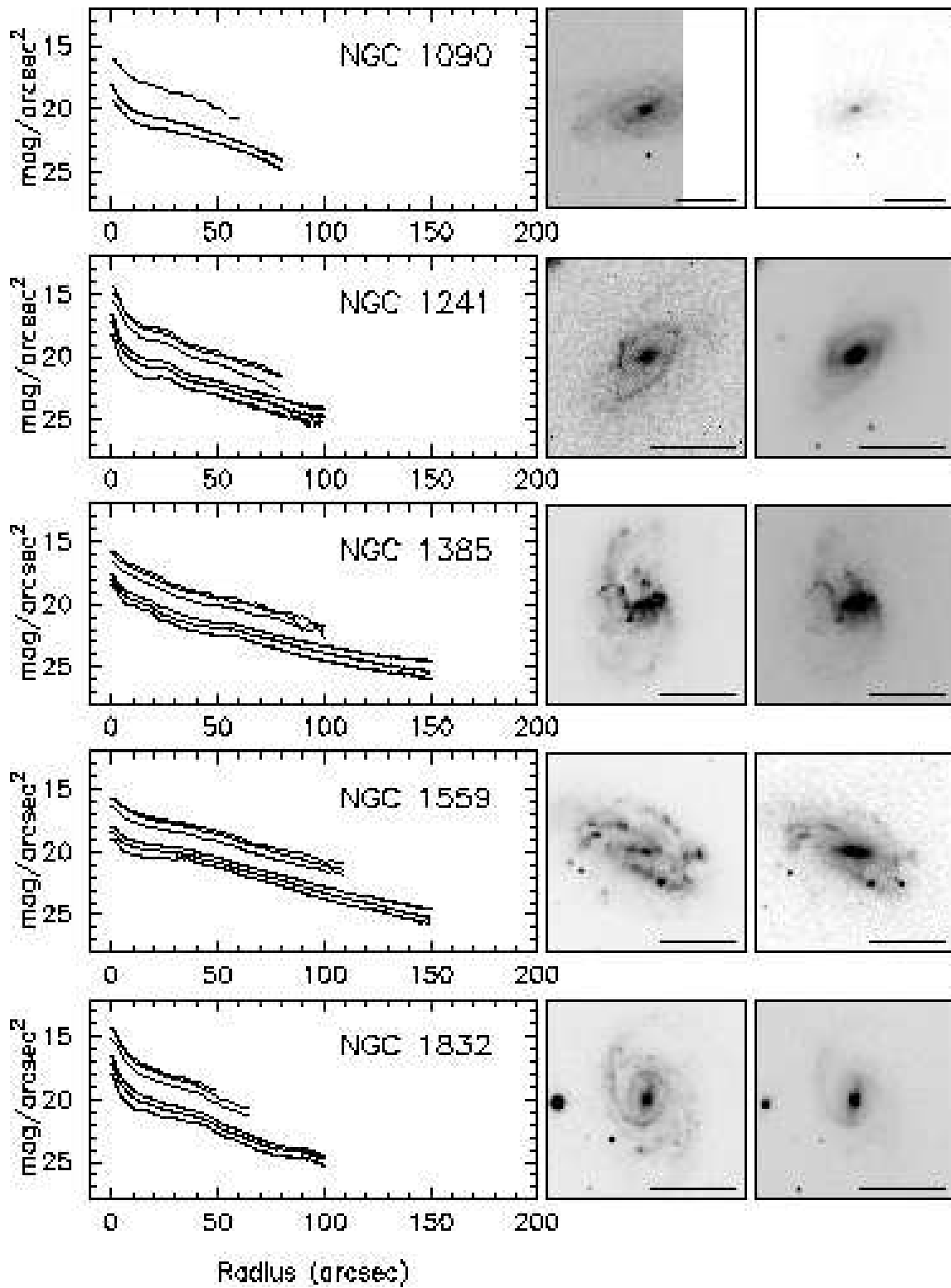


Fig. 1b.— See Figure 1a.

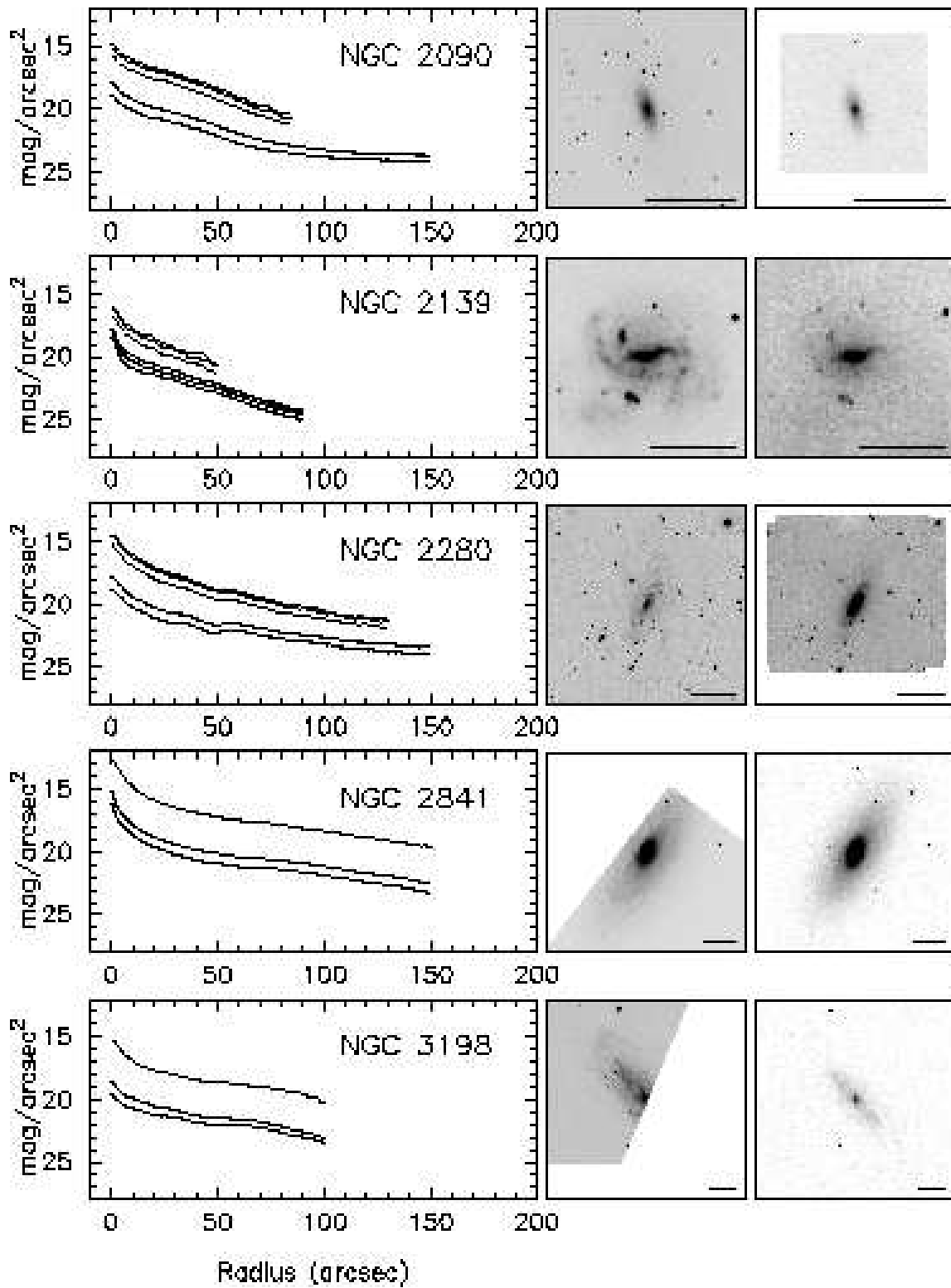


Fig. 1c.— See Figure 1a.

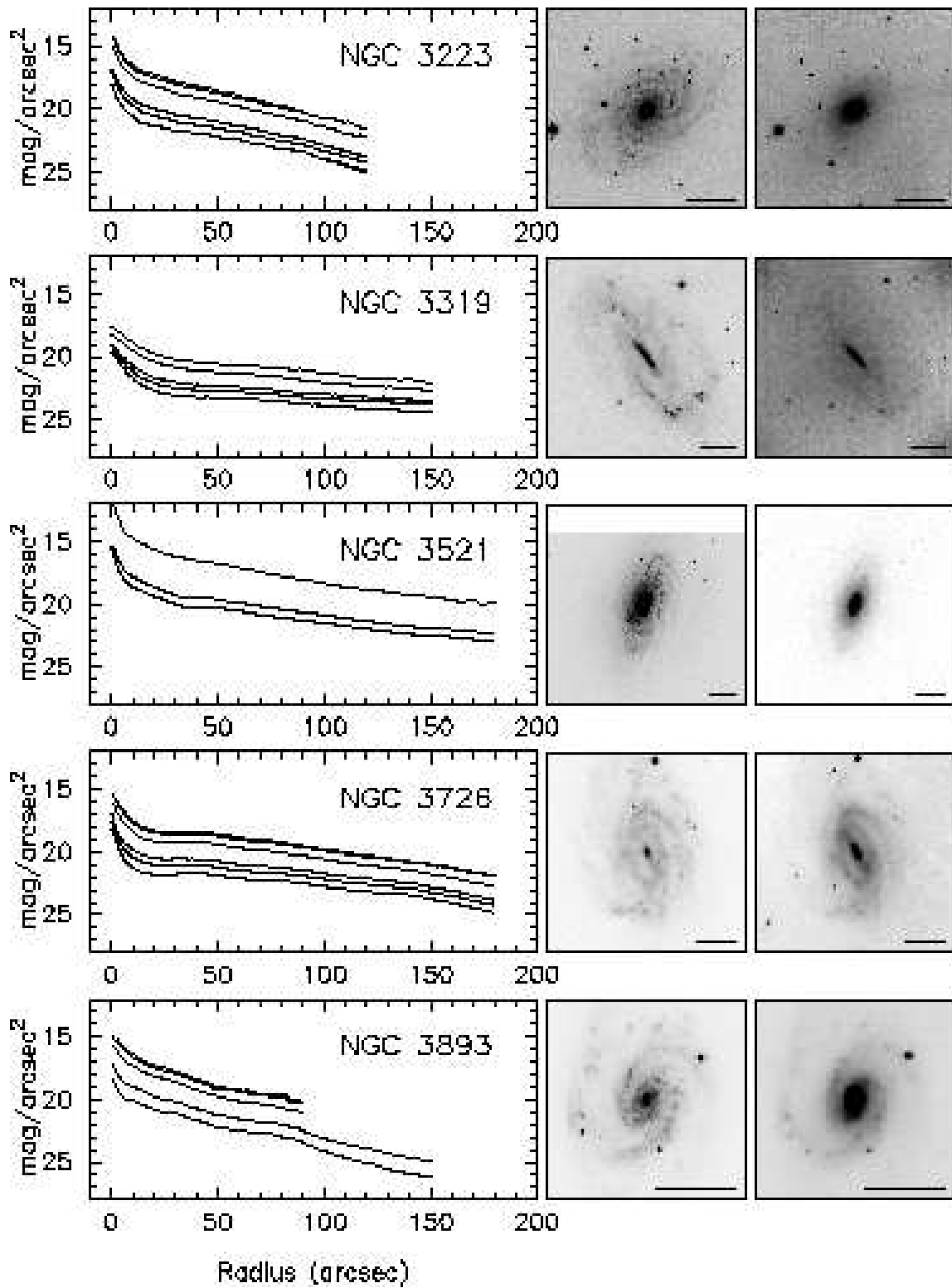


Fig. 1d.— See Figure 1a.

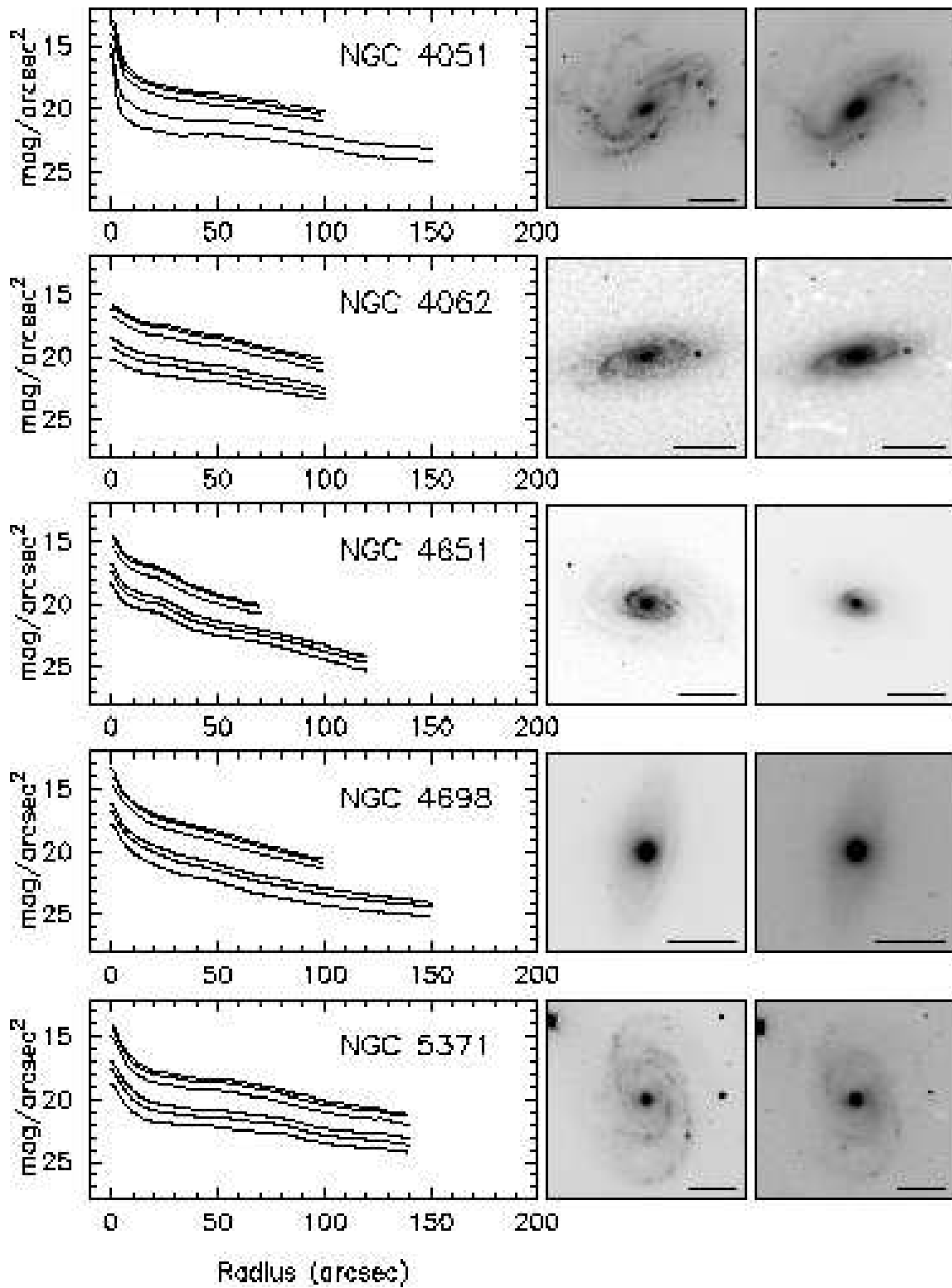


Fig. 1e.— See Figure 1a.

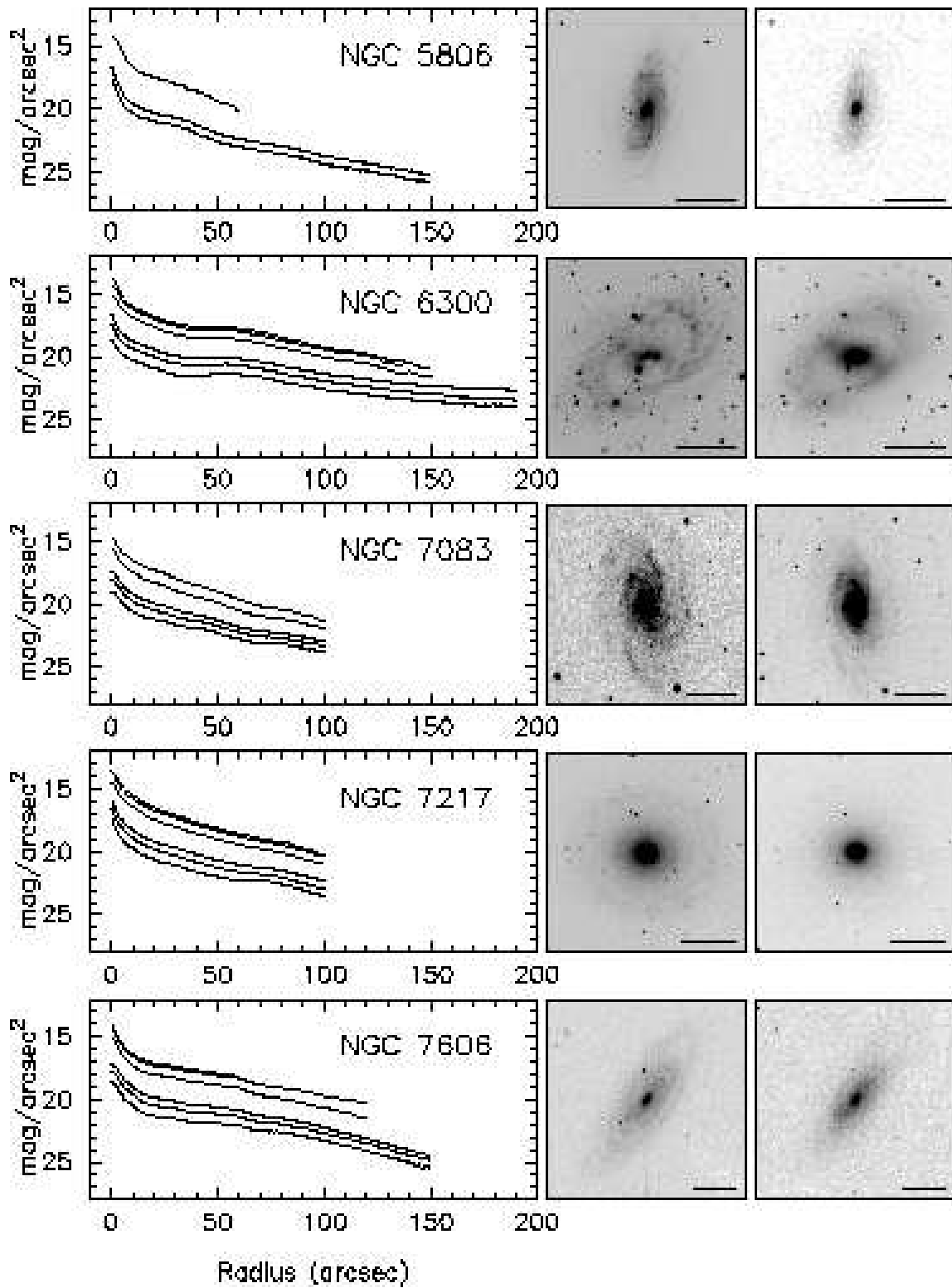


Fig. 1f.— See Figure 1a.

TABLE 1
BASIC PARAMETERS OF THE SAMPLE GALAXIES.

Galaxy	RC3 Type	D_{25} (RC3) (")	D_{25} (this paper) ^a (")	V_{hel} (km s ⁻¹)	Distance (Mpc)
NGC 157	SAB(rs)bc	250	253	1668	21.6
NGC 289	SAB(rs)bc	308	238	1628	19.9
NGC 488	SA(r)b	315	332	2272	31.0
NGC 908	SA(s)c	362	350	1498	18.9
NGC 1087	SAB(rs)c	223	219	1519	20.7
NGC 1090 ^b	SB(rs)bc	239	230	2758	37.9
NGC 1241	SB(rs)b	169	177	4052	55.5
NGC 1385	SB(s)cd	203	208	1493	19.3
NGC 1559	SB(s)cd	208	249	1292	15.8
NGC 1832	SB(r)bc	154	184	1937	27.3
NGC 2090	SA(rs)b	294	291	...	12.3 ^e
NGC 2139	SAB(rs)cd	158	171	1843	26.2
NGC 2280	SA(s)cd	379	378	1906	27.5
NGC 2841 ^b	SA(r)b	488	483	...	14.1 ^e
NGC 3198 ^b	SB(rs)c	511	298	...	14.5 ^e
NGC 3223	SA(r)bc	244	246	2895	43.6
NGC 3319	SB(rs)cd	370	364	...	14.3 ^e
NGC 3521 ^b	SAB(rs)bc	658	486	805	9.4
NGC 3726	SAB(r)c	370	398	866	21.7
NGC 3893 ^c	SAB(rs)c	268	236	967	23.6
NGC 3949 ^d	SA(s)bc	173	176	...	20.7
NGC 3953 ^d	SB(r)bc	415	424	...	20.7
NGC 3992 ^d	SB(rs)bc	455	532	...	20.7
NGC 4051	SAB(rs)bc	315	306	...	15.2
NGC 4062	SA(s)c	244	273	769	10.8 ^f
NGC 4138 ^d	SA(r)0+	144	154	...	20.7
NGC 4651	SA(rs)c	239	229	805	18.3 ^f
NGC 4698	SA(s)ab	239	241	1002	19.1 ^f
NGC 5371	SAB(rs)bc	262	320	2553	45.1
NGC 5806 ^c	SAB(s)b	185	193	1359	26.4
NGC 6300	SB(rs)b	268	430	1110	14.5
NGC 7083	SAB(rs)c	233	276	3109	40.5
NGC 7217	(R)SA(r)ab	233	224	952	15.9
NGC 7606	SA(s)b	322	279	2233	29.4

^aTypical uncertainties are ~ 5 arcsec.

^bAll imaging is from SDSS DR2 & 2MASS

^cAll imaging is from Verheijen (1997) & 2MASS

^dAll imaging is from Verheijen (1997). Distance is taken as the HST Key Project distance to the Ursa Major cluster (Sakai et al. 2000), so no heliocentric velocity is listed.

^eDistance measured from Hubble Space Telescope observations of Cepheid variable stars, so no heliocentric velocity is listed.

^fGalaxies which have a triple-valued solution for the Virgo infall calculation. The chosen solution is the one that is the closest to the calculated Tully-Fisher distance (given W_r and $H_{-0.5}$ from Tully (1988)).

TABLE 2
OBSERVATIONAL DETAILS FOR THE OSUBSGS

Galaxy	Bands	Date	Telescope	Camera	Detector
NGC 157	BVR	1995 Oct 29	CTIO 0.9m	CFCCD	Tek1K#2
	JH	1995 Oct 08	Perkins 1.8m	OSIRIS	NICMOS3
	K	2MASS
NGC 289	BVR	1995 Oct 26	CTIO 0.9m	CFCCD	Tek1K#2
	JK	1996 Oct 01	CTIO 1.5m	CIRIM	NICMOS3
	H	1996 Oct 02	CTIO 1.5m	CIRIM	NICMOS3
NGC 488	BVR	1994 Oct 11	Perkins 1.8m	IFPS	NCCD
	JHK	1995 Oct 18	Perkins 1.8m	OSIRIS	NICMOS3
NGC 908	BVR	1995 Oct 26	CTIO 0.9m	CFCCD	Tek1K#2
	JHK	1996 Sep 30	CTIO 1.5m	CIRIM	NICMOS3
NGC 1087	BVR	1993 Sep 17	Perkins 1.8m	IFPS	NCCD
	J	1995 Oct 15	Perkins 1.8m	OSIRIS	NICMOS3
	H	1995 Oct 06	Perkins 1.8m	OSIRIS	NICMOS3
	K	2MASS
NGC 1241	BVR	1995 Oct 29	CTIO 0.9m	CFCCD	Tek1K#2
	JH	1995 Oct 10	Perkins 1.8m	OSIRIS	NICMOS3
	K	2MASS
NGC 1385	BVR	1995 Oct 27	CTIO 0.9m	CFCCD	Tek1K#2
	JHK	2MASS
NGC 1559	BVR	1995 Oct 26	CTIO 0.9m	CFCCD	Tek1K#2
	JHK	1995 Mar 10	CTIO 1.5 m	CIRIM	NICMOS3
NGC 1832	BVR	1994 Nov 01	CTIO 0.9m	CFCCD	Tek2K#3
	JHK	2MASS
NGC 2090	BV	1995 Mar 07	CTIO 1.5m	CFCCD	Tek1K#2
	JHK	1995 Mar 08	CTIO 1.5m	CIRIM	NICMOS3
NGC 2139	BVR	1994 Apr 09	CTIO 0.9m	CFCCD	Tek1K#2
	JHK	2MASS
NGC 2280	BV	1995 Mar 08	CTIO 1.5m	CFCCD	Tek1K#2
	R
	JH	1995 Mar 09	CTIO 1.5m	CIRIM	NICMOS3
	K	1995 Mar 15	CTIO 1.5m	CIRIM	NICMOS3
NGC 3223	BVR	1994 Apr 07	CTIO 0.9m	CFCCD	Tek1K#2
	JHK	1994 Feb 25	CTIO 1.5m	OSIRIS	NICMOS3
NGC 3319	BVR	2000 Apr 22	MDM 1.3m	MIS	Echelle
	JH	1995 Apr 25	Perkins 1.8m	OSIRIS	NICMOS3
	K
NGC 3726	BVR	2000 Apr 26	MDM 1.3m	MIS	Echelle
	JH	1996 Mar 08	Perkins 1.8m	OSIRIS	NICMOS3
	K	1997 Mar 15	Perkins 1.8m	OSIRIS	NICMOS3
NGC 4051	BR	Verheijen
	V

TABLE 2—*Continued*

Galaxy	Bands	Date	Telescope	Camera	Detector
	JH	1996 Mar 31	Perkins 1.8m	OSIRIS	NICMOS3
	K	2MASS
NGC 4062	BVR	1996 Feb 15	Perkins 1.8m	IFPS	NCCD
	J	2MASS
	HK	1995 Mar 27	Perkins 1.8m	OSIRIS	NICMOS3
NGC 4651	BVR	1997 Mar 11	USNO	CCD	TI800
	JHK	2MASS
NGC 4698	BVR	1998 Mar 24	MDM 2.4m	MIS	Templeton
	JH	1996 Apr 29	Perkins 1.8m	OSIRIS	NICMOS3
	K	1997 Apr 07	Perkins 1.8m	OSIRIS	NICMOS3
NGC 5371	BVR	1996 Feb 15	Perkins 1.8m	IFPS	NCCD
	JHK	1995 Mar 23	Perkins 1.8m	OSIRIS	NICMOS3
NGC 6300	BVR	1996 Apr 12	CTIO 0.9m	CFCCD	Tek2K#3
	JHK	2MASS
NGC 7083	BVR	1995 Oct 26	CTIO 0.9m	CFCCD	Tek1K#2
	JK	1996 Sep 26	CTIO 1.5m	CIRIM	NICMOS3
NGC 7217	B	1994 Oct 10	Perkins 1.8m	IFPS	NCCD
	VR	1993 Sep 18	Perkins 1.8m	IFPS	NCCD
	JH	1995 Oct 18	Perkins 1.8m	OSIRIS	NICMOS3
	K	2MASS
NGC 7606	BVR	1994 Oct 11	Perkins 1.8m	IFPS	NCCD
	JHK	1994 Oct 25	CTIO 1.5m	CIRIM	NICMOS3

TABLE 3
MEASURED GALAXY PARAMETERS

Galaxy	Band	Seeing (")	Magnitude			PA (°)	<i>i</i> (°)
			total ^a	uncertainty	Literature (total)		
NGC 157	B	1.3	11.16	0.03	11.29±0.03 ^b , 11.00±0.12 ^c	43	45.6
	V	1.1	10.54	0.03	...		
	R	1.0	10.02	0.03	...		
	J	2.6	8.48		
	H	2.6	7.81		
	K	2.9	7.59		
NGC 289	B	2.0	11.05	0.03	11.72±0.13 ^c	148	49.1
	V	1.8	10.44	0.03	10.38±0.07 ^d , 10.99±0.03 ^c		
	R	1.4	10.01	0.03	...		
	J	1.9	8.81		
	H	1.5	8.24		
	K	1.6	7.98		
NGC 488	B	1.6	11.08	0.10	11.15±0.13 ^c	10	47.2
	V	1.5	10.17	0.04	...		
	R	1.8	9.57	0.07	...		
	J	2.4	7.86		
	H	2.6	7.07		
	K	2.4	6.90		
NGC 908	B	1.6	11.05	0.03	10.83±0.13 ^c	80	59.3
	V	1.1	10.37	0.03	10.18±0.13 ^c		
	R	1.2	9.81	0.03	...		
	J	1.9	8.17		
	H	2.0	7.54		
	K	2.0	7.33		
NGC 1087	B	1.9	11.71 ^e	0.05 ^e	11.46±0.12 ^c	12	50.4
	V	2.1	11.11 ^e	0.05 ^e	...		
	R	1.7	10.63 ^e	0.05 ^e	...		
	J	2.4	9.29		
	H	2.6	8.78		
	K	1.9	8.47		
NGC 1090	g	1.6	12.44 ^f	98	56.6
	r	1.6	11.64 ^f		
	K	3.3	9.24		
NGC 1241	B	3.1	12.88	0.03	11.99±0.13 ^c	128	51.7
	V	3.6	12.03	0.03	...		
	R	2.5	11.41	0.03	...		
	J	2.6	9.74		
	H	2.6	8.94		
	K	1.9	8.66		
NGC 1385	B	1.2	11.66 ^e	0.05	11.45±0.10 ^c	170	47.2

TABLE 3—*Continued*

Galaxy	Band	Seeing ($''$)	Magnitude			PA ($^\circ$)	i ($^\circ$)
			total ^a	uncertainty	Literature (total)		
NGC 1559	V	1.0	11.11 ^e	0.05	...	66	57.3
	R	1.2	10.63 ^e	0.05	...		
	J	2.0	9.25		
	H	1.9	8.66		
	K	1.9	8.40		
	B	2.1	11.11	0.03	11.00±0.30 ^c		
	V	1.8	10.64	0.03	10.65±0.30 ^c		
	R	1.6	10.21	0.03	...		
	J	1.9	8.85		
	H	2.0	8.27		
NGC 1832	K	2.0	8.05	20	48.7
	B	1.6	12.21	0.10	11.96±0.13 ^c		
	V	1.3	11.53	0.04	...		
	R	1.3	11.01	0.07	...		
	J	2.0	9.33		
	H	1.9	8.67		
NGC 2090	K	1.9	8.41	14	63.3
	B	1.5	11.74	0.05	11.99±0.13 ^c		
	V	1.4	10.94	0.04	...		
	R		
	J	2.0	8.91		
	H	2.0	8.27		
NGC 2139	K	1.9	8.02	80	39.2
	B	2.0	12.19	0.06	11.99±0.13 ^c		
	V	2.2	11.73	0.05	...		
	R	2.0	11.34	0.06	...		
	J	1.8	10.19		
	H	1.9	9.58		
NGC 2280	K	1.9	9.33	157	66.4
	B	1.2	11.80	0.15	10.90±0.20 ^c , 11.13±0.09 ^x		
	V	1.2	11.03	0.14	...		
	R		
	J	2.0	9.00		
	H	2.0	8.37		
NGC 2841	K	2.0	8.16	148	56.63
	g	1.2	9.79 ^f		
	r	1.0	9.03 ^f		
NGC 3198	K	3.1	6.13	30	60
	g	1.2	11.47 ^f		
	r	1.4	10.91 ^f		

TABLE 3—*Continued*

Galaxy	Band	Seeing (")	Magnitude			PA ($^{\circ}$)	i ($^{\circ}$)
			total ^a	uncertainty	Literature (total)		
NGC 3223	K	3.5	7.95	134	40.5
	B	1.2	11.78	0.05	11.79 ± 0.14^c		
	V	1.1	10.95	0.04	...		
	R	1.2	10.36	0.04	...		
	J	1.9	8.53		
	H	1.9	7.82		
NGC 3319	K	1.9	7.60	40	60.0
	B	1.3	11.84^e	0.07	11.48 ± 0.17^c		
	V	1.3	11.25^e	0.06	11.07 ± 0.18^c		
	R	1.4	10.94^e	0.06	...		
	J	2.4	9.96		
	H	2.4	9.36		
NGC 3521	K	163	53.13
	g	0.9	9.36^f		
	r	0.8	8.65^f		
NGC 3726	K	3.0	7.97	9	54.6
	B	1.9	10.90	0.14	10.91 ± 0.07^c		
	V	1.5	10.30	0.06	$10.62 \pm 0.02, 0.1-0.3^g$		
	R	1.1	9.81	0.09	9.97		
	J	2.4	8.63		
	H	2.6	7.94		
NGC 3893	K	2.6	7.77	172	48
	B	...	11.38	0.05	11.16 ± 0.15^c		
	V		
	R	...	10.28	0.05	...		
	J	2.4	8.72		
	H	2.4	7.98		
NGC 3949	K	2.0	7.83	117	52
	B	...	11.65	0.05	...		
	R	...	10.77	0.05	...		
NGC 3953	K	...	8.47	13	60
	B	...	11.02	0.05	...		
	R	...	9.69	0.05	...		
NGC 3992	K	...	7.00	68	56
	B	...	10.66	0.05	...		
	R	...	9.45	0.05	...		
NGC 4051	K	...	7.03	131	49
	B	...	11.28	0.05	...		
	V		
	R	...	10.15	0.05	...		

TABLE 3—*Continued*

Galaxy	Band	Seeing ($''$)	Magnitude			PA ($^\circ$)	i ($^\circ$)
			total ^a	uncertainty	Literature (total)		
NGC 4062	J	2.4	8.91	97	63.9
	H	2.4	8.36		
	K	2.6	8.00		
	B	2.6	11.86	0.09	11.9 ± 0.40^c		
	V	1.3	11.18	0.04	$11.20 \pm 0.01, \lesssim 0.05^g$		
	R	1.3	10.62	0.04	...		
NGC 4138	J	2.5	9.00	151	51.0
	H	2.6	8.37		
	K	2.6	8.13		
	B	...	12.34	0.05	...		
NGC 4651	R	...	10.79	0.05	...	82	47.9
	K	...	8.22		
	B	2.0	11.55	0.06	11.39 ± 0.08^c		
NGC 4698	V	1.9	10.81	0.04	$10.78 \pm 0.03, \lesssim 0.05^g$	168	51.3
	R	1.9	10.30	0.04	...		
	J	2.6	8.80		
	H	2.4	8.16		
	K	2.4	7.98		
	B	1.0	11.63^e	0.06	11.46 ± 0.08^c		
	V	1.0	10.67^e	0.04	...		
	R	0.9	10.14^e	0.04	...		
NGC 5371	J	2.7	8.38	16	49.8
	H	2.6	7.77		
	K	2.4	7.54		
	B	2.1	11.28	0.09	11.32 ± 0.14^c		
	V	2.0	10.55	0.04	...		
	R	2.0	9.99	0.04	...		
NGC 5806	J	2.4	8.45	170	58
	H	2.4	7.81		
	K	2.4	7.56		
NGC 6300	g	1.2	12.10	123	51.7
	r	0.8	11.37		
	K	2.7	8.46		
	B	1.1	10.80	0.05	$10.98 \pm 0.05^c, 10.98 \pm 0.02^i$		
	V	1.1	10.00	0.03	...		
NGC 7083	R	0.9	9.33	0.03	...	10	58.0
	J	1.9	7.79		
	H	1.9	7.13		
	K	1.9	6.89		
	B	2.4	11.81	0.03	11.87 ± 0.13^c		

TABLE 3—*Continued*

Galaxy	Band	Seeing (")	Magnitude			<i>PA</i> (°)	<i>i</i> (°)
			total ^a	uncertainty	Literature (total)		
NGC 7217	V	1.0	11.19	0.03	...	90	29.5
	R	1.1	10.70	0.03	...		
	J	2.0	9.20		
	H		
	K	1.9	8.28		
	B	0.9	11.26	0.10	...		
	V	0.9	10.40	0.05	...		
	R	0.9	9.74	0.07	...		
	J	2.4	7.88		
	H	2.4	7.16		
NGC 7606	K	3.6	6.93	146	63.9
	B	2.0	11.72	0.10	11.51±0.14 ^c		
	V	1.9	10.96	0.04	10.75±0.14 ^c , 10.98 ±0.01, \lesssim 0.05 ^g		
	R	2.0	10.41	0.07	...		
	J	2.0	8.61		
	H	2.0	7.79		
K	2.0	7.67			

^aUncorrected for Galactic extinction. Uncertainties in the near-infrared photometry are taken to be $\sim 4\%$.

^bFrom Ryder et al. 1998; not extinction corrected.

^cFrom the RC3; not extinction corrected.

^dFrom Walsh et al. 1997; not extinction corrected.

^eBased on a secondary calibration obtained from a short “snapshot” image taken on a photometric night

^fFor SDSS DR2 images, the zero-point calibration is accurate to $\pm 2\%$ in r and $g-r$ (Lupton et al. 2001); the sky variation in our galaxy images causes a further $\sim 2\%$ uncertainty. In total, the zero-point calibration is uncertain by $\sim 4\%$.

^gFrom Héraudeau & Simien 1996; not extinction corrected. The first error given is the rms error due to uncertainty in the sky value. The second error is the estimated accuracy in the zero-point.

^hNo stars on image to accurately measure seeing.

ⁱFrom Buta 1987; not extinction corrected.

^xFrom Lauberts & Valentijn 1989; not extinction corrected.

TABLE 4
BULGE/DISK PARAMETERS FOR *K*-BAND IMAGES

Galaxy	B/D	Bulge			Disk	
		n	R_e (arcsec)	μ_e (mag/arcsec ²)	h (arcsec)	μ_0 (mag/arcsec ²)
NGC 157 ^a	27	16.3
NGC 289	0.10	1.10	4	15.7	18	15.9
NGC 488	0.20	2.20	9	16.4	38	16.6
NGC 908 ^a	34	16.3
NGC 1087 ^a	24	16.8
NGC 1090 ^a	21	17.1
NGC 1241	0.20	1.30	4	16.0	17	16.8
NGC 1385 ^a	26	17.2
NGC 1559	0.02	1.20	3	17.1	25	16.4
NGC 1832	0.15	1.20	3	14.9	15	16.0
NGC 2090 ^a	17	15.3
NGC 2139 ^a	17	17.3
NGC 2280	0.35	1.30	12	16.9	27	16.7
NGC 2841	0.19	1.10	9	15.0	30	15.6
NGC 3198 ^a	39	17.2
NGC 3223 ^a	25	16.6
NGC 3319 ^a	72	19.8
NGC 3521	0.13	1.40	7	14.7	33	15.1
NGC 3726 ^a	45	17.4
NGC 3893	0.29	1.50	14	17.5	28	16.9
NGC 3949 ^a	16	16.1
NGC 3953 ^a	39	16.6
NGC 3992 ^a	56	17.3
NGC 4051	0.18	3.70	3	14.7	38	17.4
NGC 4062 ^a	27	16.3
NGC 4138 ^a	14	15.6
NGC 4651 ^a	16	15.7
NGC 4698	0.28	3.10	7	16.3	24	16.2
NGC 5371	0.11	1.30	5	15.7	37	17.0
NGC 5806	0.20	1.40	4	15.3	19	16.3
NGC 6300	0.09	1.20	6	15.9	30	16.2
NGC 7083	0.06	1.50	3	15.7	16	15.8
NGC 7217	24	15.7
NGC 7606	31	16.3

^aFor galaxies with a negligible bulge component we fit an exponential disk, and hence we only list the central surface brightnesses and scalelengths of the disks.